Compact-Polarimetry for oil basins observation

Rafael Lemos Paes[1]
Andrea Buono[2]
Ferdinando Nunziata[2]
Maurizio Migliaccio[2]
João Antonio Lorenzzetti[1]

[1] Instituto Nacional de Pesquisas Espaciais (INPE), Earth Observation Coordination
12227-010, São José dos Campos - SP, Brazil
rlpaes, loren@dsr.inpe.br

[2] Dipartimento di Ingegneria, Università degli Studi di Napoli Parthenope
Centro Direzionale, isola C4, 80133 – Napoli, Italy
andrea.buono, ferdinando.nunziata, maurizio.migliaccio@uniparthenope.it

Abstract. In this study, Compact-Polarimetry (CP) Synthetic Aperture Radar (SAR) architectures are exploited for oil basins observation purposes. Basic wave polarimetry concepts are used to define the considered CP features emulating actual C-band fully polarimetric SAR data. Oil basins represent an interesting scenario from both an environmental and economical perspective. They are a very complex marine environment in which there are metallic targets together with potential oil slicks that cover sea surface. Meaningful experiments undertaken emulating RADARSAT-2 SAR data demonstrate the capability of CP architectures to both detect metallic targets at sea and monitor oil slicks. To address target and oil slick detection simultaneously, a Principal Component Analysis (PCA) is first performed to reduce the space of the considered CP features. Hence, once selected the most suitable set of features to be used in the ocean/target/oil classification process, an empirical global threshold choosen accordingly to image statistics is adopted to highlight the presence of metallic targets and oil slicks over the sea clutter. Then, once both metallic targets and oil slicks are sorted out from the ocean background using an adaptive approach involving norm calculation and based on local thresholds, to solve challenging cases in which they call for similar feature values, results obtained by processing the CP features are combined with the intensity information. Furthermore, oil characterization is addressed with a statistical analysis supported by an Euclidean metric to quantify the separation between oil slick and sea histograms.

Keywords: synthetic aperture radar, compact polarimetry, oil basins .

1. Introduction

Oil basins represent a very complex marine scenario in which moving and fixed metallic targets (ships, tankers, oil rigs, pipelines and drilling platforms) having a different size, shape and structure are at sea together with oil slicks covering sea surface. Hence, since all matters are related to surveillance for navigation security, anti-piracy activities, maritime traffic control, etc., a key issue is not only the spatial surveillance coverage but also the temporal revisit time. In this sense, satellite Synthetic Aperture Radar (SAR) represents a fundamental tool since it is a synoptic active microwave system whose imaging capabilities are independent on solar illumination and mostly unaffected by weather conditions. Basically, in single-polarization SAR imagery targets result in bright spots while oil slicks appear as dark areas. Unfortunately, several marine features as low-wind areas, atmospheric fronts, biogenic thin natural films and ship's wakes, termed look-alikes, appear in the same way producing misclassifications. However, a review of the state-of-art of polarimetric SAR-based ship detection and of remote sensing-based oil pollution monitoring can be found in

(ZHAOYING; JINSONG, 2004; SOLBERG, 2012). Fully polarimetric (FP) SAR architecture comes at high costs in terms of average transmitted power, halved swath width and limited range of acceptable incidence angles with respect to a single-/dual-polarization SAR. Nevertheless, such FP SAR drawbacks can be overcome by the Compact-Polarimetry (CP) architectures. The main idea of CP SAR architectures is to transmit only one polarization while receiving coherently, according to an orthogonal polarization basis. Among them, varying the transmitting/receiving polarization couple, it can be obtained different architectures: Hybrid-Polarity (HP), Linear (LIN) and Circular-Circular (CC), that will be described in Subsection 2.2. Specific advantages of CP SAR architectures can be found in (SOUYRIS et al., 2007; RANEY, 2007; RANEY et al., 2011; ATTEIA; COLLINS, 2013). In this study, emulated CP SAR data obtained transforming actual FP SAR measurements are exploited to observe oil basins simultaneously monitoring metallic targets and oil slicks. In detail, once selected the most suitable set of features to be used in the ocean/target/oil classification process using a Principal Component Analysis (PCA), oil-target/ocean discrimination is addressed using an adaptive thresholding algorithm based on norm computation. Then, the final output is easily obtained using global thresholds set accordingly to image statistics or intensity information. Furthermore, oil/look-alike characterization is accomplished measuring the Euclidean distance between normalized histograms. Experimental results demonstrate that CP features are able to distinguish both targets and oil slicks from the ocean background, providing a reliable separation between oil slicks and metallic targets, and to discriminate oil slicks from look-alikes. The remainder of this paper is organized as follows: Section 2 presents the considered CP architectures and the polarimetric features; Section 3 shows the results and the discussion about experiments, while proper conclusions are drawn in Section 4.

2. Theoretical Background

2.1. Wave Polarimetry and Polarimetric Features

In real scenarios, since electric waves scattered off a distributed scene in response to an almost monochromatic illumination show partially polarized properties ranging between fully polarized and unpolarized wave ones, their description relies on second-order field correlation properties that can be obtained using the coherence matrix, ((GIL, 2007) and the references within). The 2x2 coherence matrix $\mathbf{\Gamma}$ is Hermitian and semipositive defined, and its components along an orthogonal x-y basis are given by:

$$\mathbf{\Gamma} = \langle \mathbf{E}\mathbf{E}^\dagger \rangle = \begin{pmatrix} \langle E_x E_x{}^* \rangle & \langle E_x E_y{}^* \rangle \\ \langle E_y E_x{}^* \rangle & \langle E_y E_y{}^* \rangle \end{pmatrix} = \begin{pmatrix} \Gamma_{xx} & \Gamma_{xy} \\ \Gamma_{yx} & \Gamma_{yy} \end{pmatrix} \tag{1}$$

where, $\mathbf{E}$ is the complex electric field; $\dagger$ and * stand for complex conjugate transpose and complex conjugate, respectively; a temporal dependence $e^{j\omega t}$ is considered, where ω is the angular frequency, j is the imaginary unit, and t stands for time. The correlation prevailing between the orthogonal components of the electric field is represented by the off-diagonal elements of $\mathbf{\Gamma}$. Hence, the complex correlation coefficient μ_{hv} can be defined as:

$$\mu_{hv} = |\mu_{hv}|e^{j\delta_{hv}} = \frac{\Gamma_{xy}}{\sqrt{\Gamma_{xx}}\sqrt{\Gamma_{yy}}} \quad ; \quad 0 \leq |\mu_{hv}| \leq 1 \; , -180° \leq \delta_{hv} \leq +180° \tag{2}$$

where, δ_{hv} is the phase difference between the components x and y of the electric field. When the wave is unpolarized, $\mu_{hv} = 0$, while a fully polarized wave presents $|\mu_{hv}| = 1$. Basis invariant compact parameters used to describe the state of polarization as well as the degree of randomness of a generic partially polarized wave are the degree of polarization p and the

wave entropy H_w. They can be physically understood as a measure on how close the wave is fully polarized and on how far the electric field is from being completely random. They are mathematically given by ((GIL, 2007) and the references within):

$$p = \sqrt{1 - \frac{4det(\mathbf{\Gamma})}{tr(\mathbf{\Gamma})^2}} \quad , \; H_w = -tr(\hat{\mathbf{\Gamma}}log_2\hat{\mathbf{\Gamma}}) \; ; \; 0 \leq p, H_w \leq 1 \tag{3}$$

where $\hat{\mathbf{\Gamma}} = \frac{\mathbf{\Gamma}}{tr(\mathbf{\Gamma})}$. $p = 0$ ($H_w = 1$) means totally unpolarized while $p = 1$ ($H_w = 0$) fully polarized wave. Additionally, in this study the circular polarization ratio μ_c is also used which is given by (RANEY et al., 2012; SHIRVANY; CHABERT; TOURNERET, 2012):

$$\mu_c = \frac{\Gamma_{yy} + \Gamma_{xx} - 2\Im(\Gamma_{xy})}{\Gamma_{yy} + \Gamma_{xx} + 2\Im(\Gamma_{xy})} \geq 0 \tag{4}$$

where $\Im(\cdot)$ stands for imaginary part and μ_c is the ratio of the same-sense to opposite-sense circular polarization received power, performing a measure of volumetric multiple scattering. These features have been first used for ship detection in (PAES; NUNZIATA; MIGLIACCIO,) and for oil slick observation in (NUNZIATA; MIGLIACCIO; LI, 2014).

2.2. CP SAR Architectures

HP architecture consists of transmitting a circularly polarized wave while receiving coherently two orthogonal linear H and V polarizations (RANEY, 2007). In this study, a RH circular polarization transmission is assumed. The linearly polarized received field $\mathbf{E_{HP}} = (E_h, E_v)$ is emulated by the fully polarimetric scattering matrix $\mathbf{S}$ according to (RANEY et al., 2011; PAES; NUNZIATA; MIGLIACCIO,):

$$\mathbf{E_{HP}} = \begin{pmatrix} E_h \\ E_v \end{pmatrix} = \frac{1}{\sqrt{2}} \begin{pmatrix} S_{hh} - jS_{hv} \\ S_{hv} - jS_{vv} \end{pmatrix} \tag{5}$$

where, S_{pq} with $p, q \in \{H, V\}$ is the complex scattering amplitude. Then, the HP features can be emulated by wave polarimetry concepts using the following relationships between the elements of $\mathbf{S}$ and $\mathbf{\Gamma}$ (eq. (1)):

$$\begin{array}{c} \Gamma_{hh} = \frac{1}{2}(|S_{hh}|^2 + |S_{hv}|^2 + jS_{hh}S_{hv}{}^* - jS_{hv}S_{hh}{}^*) \\ \Gamma_{hv} = \frac{1}{2}(S_{hh}S_{hv}{}^* + jS_{hh}S_{vh}{}^* - j|S_{hv}|^2 + S_{hv}S_{vv}{}^*); \; \Gamma_{vh} = \Gamma_{hv}{}^* \\ \Gamma_{vv} = \frac{1}{2}(|S_{hv}|^2 + |S_{vv}|^2 + jS_{hv}S_{vv}{}^* - jS_{vv}S_{hv}{}^*) \, . \end{array} \tag{6}$$

Since for CP-LIN architecture a linearly polarized wave oriented at $+45°$ in the H-V plane instead of a circularly polarized field is transmitted, its $\mathbf{\Gamma}$ matrix of eq. (1) can be obtained in a completely similar way considering the following linearly polarized received field $\mathbf{E_{CP-LIN}} = (E_h, E_v)$ (SHIRVANY; CHABERT; TOURNERET, 2012):

$$\mathbf{E_{CP-LIN}} = \begin{pmatrix} E_h \\ E_v \end{pmatrix} = \frac{1}{\sqrt{2}} \begin{pmatrix} S_{hh} + S_{hv} \\ S_{hv} + S_{vv} \end{pmatrix} \tag{7}$$

Considering a CP-CC architecture, since it consists of transmitting a RH circularly-polarized field while receiving coherently in an orthogonal circular RH-LH basis, the circularly-polarized field $\mathbf{E_{CP-CC}} = (E_{rhc}, E_{lhc})$ received at the SAR antenna can be emulated as (SHIRVANY;

CHABERT; TOURNERET, 2012):

$$\mathbf{E_{CP-CC}} = \begin{pmatrix} E_{rhc} \\ E_{lhc} \end{pmatrix} = \frac{1}{\sqrt{2}} \begin{pmatrix} 1 & j \\ j & 1 \end{pmatrix} \mathbf{E_{HP}} = \frac{1}{2} \begin{pmatrix} S_{hh} + S_{vv} \\ 2S_{hv} + jS_{hh} - jS_{vv} \end{pmatrix} \tag{8}$$

obtained considering the similar transformation required for rotate the field defined in eq. (5) into the circular basis. Thus, the quantitative parameters previously presented ($|\mu_{hv}|$, δ_{hv}, H_w, p and μ_c) can be derived for all the CP SAR architectures.

3. Experiments

In this section, meaningful experiments undertaken over actual C-band fully polarimetric RADARSAT-2 SAR data are shown to demonstrate the capability of CP SAR architectures to be used for oil basins monitoring purposes. A Single-Look Complex (SLC) acquisition (product ID: PDS_01141690) gathered on 15 May 2010 at 11:50:22 UTC, off the Lousiana Coasts in the Gulf of Mexico (29.72°N, 89.08°W), is considered. Well-known oil slicks due to the Deepwater Horizon accident and metallic targets as oil rigs and ships involved in cleaning-up operations were present into the observed scene at the time of the acquisition (ground truth provided by the Minerals Management Service, 2009) and moderate wind conditions apply (4-7 m/s) (MIGLIACCIO et al., 2011). All the CP features considered in this study, obtained emulating real SAR measurements from the Γ matrix of eq. (1), are processed applying a 7x7 average moving window. A 2854x3345 excerpt of the original 7853x3369 SAR image is shown in Fig. 1(a), where the gray-tone VV intensity channel image is shown in logaritmic scale. A second SLC RADARSAT-2 SAR acquisition (product ID: PDS_00886040) is then considered to analyze the capability of CP architectures to discriminate oil slicks from look-alikes. In fact, in the 6305x2492 image gathered on 14 December 2009 at 14:09:15 UTC off the California Coast (34.30°N, 119.80°W), in Santa Barbara Channel, a weak damping marine feature most likely due the produced-water discharge of the oil rig is clearly visible as shown in the 610x293 SAR image excerpt of Fig. 1(b) (NUNZIATA; MIGLIACCIO; GAMBARDELLA, 2011),(NUNZIATA; GAMBARDELLA; MIGLIACCIO, 2012). It can be noted that the elongated shape and the position of the marine feature makes this one a very challenging case, in which such a look-alike can be easily confused with a ship's wake.

Hence, the sensitivity of each polarimetric feature with respect to both metallic targets and oil slicks over the ocean surface is investigated. In Fig. 1(c)-(f) results related to the CP features extracted from the first acquisition are shown for the HP architecture, where the one related to p is not shown due to its complementarity with H_w. From a first visual inspection, they all witness the capability to highlight the presence of both targets and oil slicks over the ocean clutter. However, since from a visual inspection the other CP SAR architectures considered in this study provided similar results, they are not shown to save space. To provide a deeper analysis, the simultaneous detection of oil and targets is first accomplished performing a PCA to reduce the space of the considered CP features. Among them, p, H_w and $|\mu_{hv}|$ are selected since they all measure, although in different ways, the degree of depolarization of the backscattered field polarization state, thus carrying on similar polarimetric information. The correlation performed between each CP feature and the first Principal Component (PC) confirms that consideration, indicating in p (or H_w or $|\mu_{hv}|$), δ_{hv} and μ_c the features set that most contributes for that PC. Hence, emphasizing the presence of metallic targets and oil slicks over the ocean background while avoiding single-polarization issues, i.e., false alarms caused by small heterogeneities at sea, is addressed using an adaptive thresholding approach based on individuating ocean sub-regions that contain target or oil pixels. The latter is performed through norm computation, which procedure is shown in Fig. 2(a). Nonetheless, to solve challenging cases in which

oil regions and target pixels are undistinguishable since they call for very similar CP feature values, the empirical global threshold to be set for achieving the final classication output can be selected integrating the intensity information provided by SAR measurements. In fact, in single-polarization SAR imagery oil slicks and metallic targets appear very different, as dark areas and bright spots respectively. However, following the processing chain shown in Fig. 2(a), the CP features set composed by p, δ_{hv} and μ_c is tested to provide the best oil-target/sea discrimination. The output of the processing chain reported in Fig. 2(a) are shown in Fig. 2(b) and (c) for μ_c. It can be noted that μ_c achieves good performance, also allowing the detection of a metallic target within an oil region (see 2(c)) using a global threshold equal to 0.7. However, it still presents a limitation for some targets, i.e., targets exhibiting low-to-moderate volumetric information due to their structure or geometry can be misclassified as oil. Moreover, since in this case oil and target call for p values very close to each other (see also Fig. 3(c)), the global threshold required to produce the final output has to be set according to the HH channel intensity values (threshold equal to 0.07, not shown to save space). In fact, although from this point of view the HH channel represents the worst case being, among all the single polarization channels, the one for which the target and oil electromagnetic response is the closest, it easily provides a clear separation.

To support such analysis, the sensitivity of CP features to both metallic targets and oil slicks is evaluated considering their behaviour along a transect (see green dashed line in Fig. 1(a)). It is clear that all the features, for all the three different CP SAR architectures considered in this study, allow to emphasize the presence of targets and oil slicks over the ocean background (see left side of Fig. 3). Furthermore, it is important to underline that μ_c (Fig. 3(b)), being related to volumetric information, is characterized by a different sensitivity for metallic targets and oil slicks while δ_{hv} (Fig. 3(a)) is highly sensitive to both target and oil phase random variations (LI et al., 2013) providing no characteristic pattern to be recognized. p is feasible but it is not always able to distinguish targets from oil, showing an oil pattern within the same range of values of those for targets (see Fig. 3(c)). On the right side of Fig. 3, normalized histograms computed for the CP SAR architectures over two Region Of Interests (ROI)s belonging to an oil slick-free and an oil slick-covered sea surface area (see Fig. 1(a)) are shown. Please note that for p (and H_w values, not shown for the sake of brevity as well as for $|\mu_{hv}|$), being a basis invariant parameter, the analysis for CP-CC architecture is the same that for the HP one. The slick-free and the slick-covered sea empirical distributions are practically not overlapped, witnessing the capability of CP architectures to observe oil slicks at sea. To quantitative measure the degree of separability between sea and oil histograms, the Euclidean distance, defined as $\sqrt{\left(\sum_{i=1}^{N}(h_{oil}-h_{sea})^2\right)}$, over 1000 ROI samples is accomplished considering N=100 bins (see the right side of Fig. 3). In an Euclidean metric space higher values mean a larger degree of separability between histograms. The very high values for δ_{hv} are due to the shape of its distribution (same mean but different variance for oil and sea), the Euclidean distance being a bin-to-bin measure. However, the variability and statistical analysis performed, which results are summarized in Fig. 3, can be also useful to set the global thresholds (see Fig. 2(a)).

Then, to demonstrate the capability of CP architectures to discriminate oil slicks from weak damping look-alikes, the SAR image excerpt of Fig. 1(b) is considered. Experimental results are shown in Fig. 4. The latter, on the left side, shows the behaviour of the considered CP features, not shown for the sake of brevity, emulated from HP architecture along the oil rig and the dark area transects highlighted in Fig. 1(b) with a blue and red dashed line, respectively. The large peak values along metallic target pixels can be clearly noted (see blue dashed circles in Fig. 4), as well as the slightly larger values along the marine feature pixels with respect to the ocean background. In particular, δ_{hv} reveals no variations over the marine feature area, behaving

as over a slick-free sea one. Since the other CP architecture provided similar results, they are not shown to save space. A visual inspection of the right side of Fig. 4 witnesses the higher degree of overlapping between slick-free and weak damping slick-covered sea normalized histograms, also confirmed by the Euclidean distance measures. This suggests that look-alikes behaviour is almost the same that for the ocean surface since they both call for a Bragg scattering mechanism. However, since the Euclidean metric is a bin-to-bin distance, anomalies can occur (slightly larger, with respect to oil values, look-alike Euclidean distances for μ_c and δ_{hv} in the CP-LIN and CP-CC architectures, respectively).

4. Conclusions

In this study, CP SAR architectures are exploited for oil basins observation purposes. Experiments are undertaken emulating CP SAR data from actual C-band fully polarimetric RADARSAT-2 SAR measurements. Fundamentals of wave polarimetry are used to define a set of CP features: $|\mu_{hv}|$, δ_{hv}, μ_c, H_w and p. Experimental results demonstrated the capability of CP architectures to perform an oil/target/ocean classification using empirical global thresholds and to distinguish oil slicks from weak damping look-alikes. PCA is used to identify the most reliable set of CP features allowing a clear discrimination between oil and target areas from the sea background, as well as the one between metallic targets and oil slicks. Furthermore, a quantitative analysis based on an Euclidean metric between the normalized histograms proved the capability of CP features to distinguish oil slicks from look-alikes.
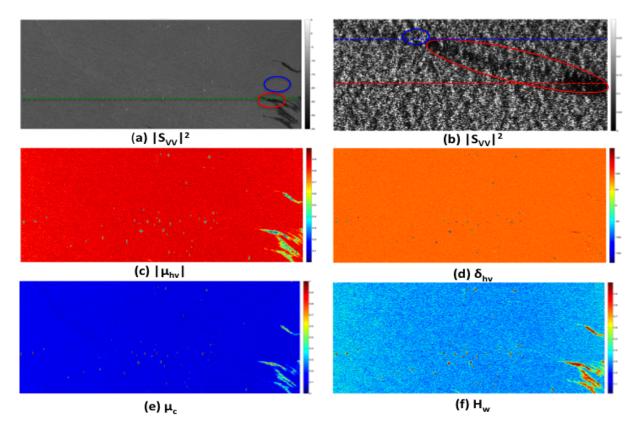

Figura 1: (a), (b): VV intensity images of the considered excerpts referred to the C-band RADARSAT-2 full-pol SAR data for oil/target processing (logaritmic scale) and for oil/look-alike classification (linear scale), respectively. In (a) oil and sea ROIs used for statistical processing are highlighted in red and blue circles, respectively, while the green dashed line represents the considered transect. In (b) the oil rig is highlighted with a blue circle and the marine feature is within the red ellipsoid. The considered transects for oil rig and look-alike are shown with a blue and red dashed line, respectively. HP features: (c) $|\mu_{hv}|$ image, (d) $\delta_h v$ image, (e) μ_c image, (f) H_w image.
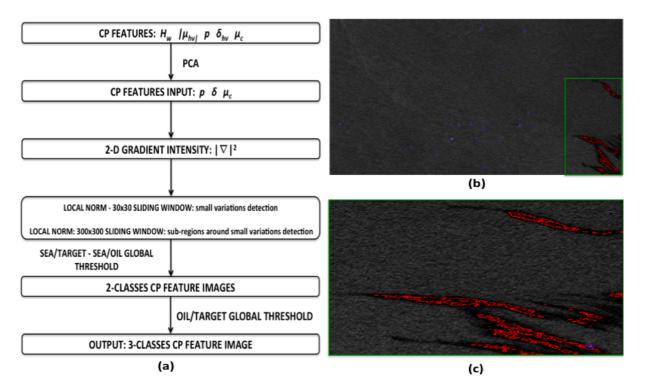
Figura 2: Classification output results. (a) Sketch of the block diagram referred to the oil/target/sea classification algorithm used. (b) μ_c-based output superimposed over the VV intensity channel image (threshold equal to 0.7 set accordingly to to its behaviour along the transect), in which regions belonging to target and oil classes are shown in blue and red, respectively. (c) Enlarged version of μ_c output image shown in (b) referred to the region in the green rectangle, where the detected ship, in blue, is cleary visible within the oil region, in red.
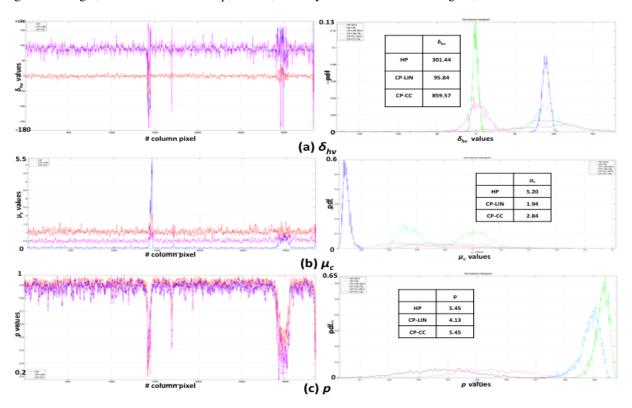

Figura 3: On the left side, the behaviour of the CP features along the transect shown in Fig. 1(a) are shown for the considered SAR architectures. On the right side, the normalized histograms for slick-free and slick-covered sea samples belonging to the ROIs considered in Fig. 1(a), for the three different SAR architectures, are shown together with the corresponding values of the Euclidean distance. (a) δ_{hv}, (b) μ_c and (c) p images.
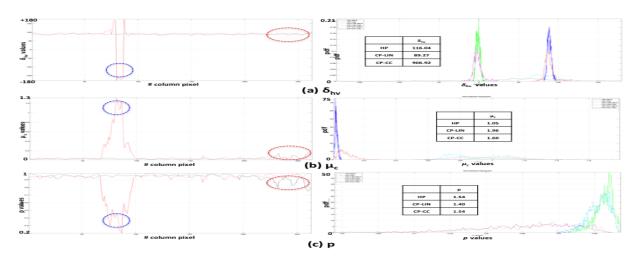
Figura 4: On the left side, the behaviour of the HP features along the transects shown in Fig. 1(b), for which the red line refers to the blue transect and the black line to the red one. In blue and red dashed circles the presence of the oil rig and the look-alike is highlighted, respectively. On the right side, normalized histograms for slick-free sea and look-alike samples, for the three different SAR architectures, are shown together with the corresponding values of the Euclidean distance. Results referred to (a) δ_{hv}, (c) μ_c and (d) p.

Referências

ATTEIA, G. E.; COLLINS, M. J. On the use of compact polarimetry sar for ship detection. *ISPRS Journal of Photogrammetry and Remote Sensing*, v. 80, p. 1–9, 2013.

GIL, J. J. Polarimetric characterization of light and media. *The European Physical Journal Applied Physics*, v. 40, n. 1, p. 1–47, 2007.

LI, H. et al. Target detection on the ocean with the relative phase of compact polarimetry sar. *IEEE Trans. Geosci. Remote Sens.*, v. 51, n. 6, p. 3299–3305, 2013.

MIGLIACCIO, M. et al. Marine added-value products using radarsat-2 fine quad-polarization. *Can. J. Remote Sens.*, v. 37, n. 5, p. 443–451, 2011.

NUNZIATA, F.; GAMBARDELLA, A.; MIGLIACCIO, M. A unitary mueller-based view of polarimetric sar oil slick observation. *IJRS Int. J. Remote Sens.*, v. 33, n. 20, p. 6403–6425, 2012.

NUNZIATA, F.; MIGLIACCIO, M.; GAMBARDELLA, A. Pedestal height for oil spill observation. *IET Radar Sonar and Navigat.*, v. 5, n. 2, p. 103–110, 2011.

NUNZIATA, F.; MIGLIACCIO, M.; LI, X. Sea oil slick observation using hybrid-polarity sar architecture. *J. Ocean. Engin.*, PP, n. 99, p. 1–15, 2014.

PAES, R. L.; NUNZIATA, F.; MIGLIACCIO, M. On the capability of hybrid-polarity features to observe metallic targets at sea. Submitted on J. Ocean. Engin., 2014.

RANEY, R. K. Hybrid-polarity sar architecture. *IEEE Trans. Geosci. Remote Sens.*, v. 45, n. 11, p. 3397–3404, 2007.

RANEY, R. K. et al. The m-chi decomposition of hybrid dual-polarimetric radar data with application to lunar craters. *J. Geophys. Res.*, v. 117, n. 21, 2012.

RANEY, R. K. et al. The lunar mini-rf radars: hybrid polarimetric architecture and initial results. In: *Proceedings of IEEE*. [S.l.: s.n.], 2011. v. 99, n. 5, p. 808–823.

SHIRVANY, R.; CHABERT, M.; TOURNERET, J. Ship and oil-spill detection using the degree of polarization in linear and hybrid/compact dual-pol sar. *J. Sel. Topics Appl. Earth Observ.*, v. 5, n. 3, p. 885–892, 2012.

SOLBERG, A. H. S. Remote sensing of ocean oil-spill pollution. In: *Proceedings of the IEEE*. [S.l.: s.n.], 2012. v. 100, n. 10, p. 2931–2945.

SOUYRIS, J. C. et al. Sar compact polarimetry (cp) for earth observation and planetology: concept and challenges. In: POLINSAR. Frascati: ESA-ESRIN, 2007.

ZHAOYING, H.; JINSONG, C. D. A review of ship detection algorithms in polarimetric sar images. In: 7TH INTERNATIONAL ICSP. *Signal Processing*. [S.l.], 2004. v. 3, p. 2155–2158.